Determination of the magnetic particle distribution in tumour tissue by means of x-ray tomography



2006 J. Phys.: Condens. Matter 18 S2903

(http://iopscience.iop.org/0953-8984/18/38/S25)

INSTITUTE OF PHYSICS PUBLISHING JOURNAL OF PHYSICS: CONDENSED MATTER

J. Phys.: Condens. Matter **18** (2006) S2903–S2917 doi:10.1088/0953-8984/18/38/S25

# Determination of the magnetic particle distribution in tumour tissue by means of x-ray tomography

**O Brunke[1], S Odenbach[1], R Jurgons[2], C Alexiou[2], I Hilger[3] and F Beckmann[4]**

[1] TU Dresden, Lehrstuhl für Magnetofluiddynamik, 01062 Dresden, Germany
[2] Klinik und Poliklinik für Hals-, Nasen- und Ohrenkranke, Universitätsklinikum Erlangen, Germany
[3] Institut für Diagnostische und Interventionelle Radiologie, FSU Jena, Germany
[4] GKSS-Forschungszentrum Geesthacht, Max-Planck-Straße 1, 21502 Geesthacht, Germany

E-mail: Oliver.Brunke@tu-dresden.de

Received 13 June 2006, in final form 5 July 2006
Published 8 September 2006
Online at stacks.iop.org/JPhysCM/18/S2903

**Abstract**

In biomedical applications of ferrofluids, the resulting distribution of the magnetic nanoparticles is a crucial parameter for the effect of the therapeutic approach. In order to increase the efficacy of local cancer treatments incorporating ferrofluids like magnetic drug targeting and hyperthermia, the biodistribution of theses fluids in the respective tissue has to be optimized. Usually, the distribution of particles is determined by histological cuts of the investigated specimen, a technique which provides only local information about the overall distribution of the magnetic material, e.g. in a tumour. Radioscopic techniques based on gamma or x-rays are well established, suitable for *in vivo* examination and non-destructive, but only provide two-dimensional integral information in the direction of the beam. Here we have used micro-tomography—incorporating a conventional x-ray tube as well as monochromatic synchrotron radiation—as a tool for a three-dimensional analysis of the distribution of magnetic nanoparticles in biological applications. Compared to biological matter, the iron-based magnetic nanoparticles provide sufficiently high absorption for x-rays and thus serve as an intrinsic contrast agent for the examinations. The results show the principle feasibility of the method for a quantitative determination of the agglomeration behaviour of the nanoparticles within carcinogenic tissue after intravascular or intratumoural injection.

(Some figures in this article are in colour only in the electronic version)

## 1. Introduction

A number of research activities in recent years have shown the high potential of ferrofluids for biomedical applications. Of major interest, in particular, are the uses of magnetic nanoparticles as a biocompatible contrast agent for diagnostic purposes, especially in the field

  

of cancer treatment. Magnetic drug targeting [1, 2] is the approach for directly delivering chemotherapeutic drugs which are bonded ionically to magnetic nanoparticles to the tumour by means of a strong magnetic field gradient. By means of hyperthermia [3], local heating of tissue is achieved by exciting magnetic nanoparticles which have been injected at a specific location with an external alternating magnetic field.

Both approaches offer local treatment of the carcinogenic tissue, which could reduce side-effects compared to conventional therapies. However, detailed information about the particle distribution is of severe importance. In order to minimize side effects during drug targeting, it is desirable, for example, to direct the chemotherapeutics as close as possible to the region of the carcinogenic tissue. Additionally, the efficiency and success of the therapeutic approach strongly depends on the intratumoural distribution. In order to qualify the success of the therapeutic approach, it is therefore required to determine the spatial particle distribution within the tumour and the surrounding region. This information is furthermore required for the modelling of heat generation in hyperthermia and thus for effective development of this therapeutic tool.

In this context, current radiological imaging procedures are related to a variety of limitations, i.e. in terms of spatial image resolution and the ability to determine quantitative information, for instance the particle concentration. The commonly used two-dimensional (2D) radiographic techniques, e.g. incorporating x-rays or gamma-rays, furthermore generally only provide integral information about the content of magnetic material along the beam direction. On the other hand, the applicability of histology is not suitable during the therapeutic procedure due to its destructive nature. Moreover, this technique only shows a relative local snapshot of the magnetic particle distribution, limited by the number of histological cuts taken from the specimen examined.

For such means, a three-dimensional (3D) mapping of the distribution as well as concentration of magnetic particles with high spatial resolution is required. Modern three-dimensional imaging techniques like x-ray micro-computed tomography ($\mu$CT) offer a non-destructive way to determine the complete 3D spatial morphology of the specimen. The present paper is intended to show the feasibility of this method for analysis of the structure of carcinogenic tissue enriched with magnetic nanoparticles. In the first part, a brief review of the basic principles of two therapeutic approaches—magnetic drug targeting and hyperthermia—is given.

In section 3 the two tomographic systems are introduced. A small, self-assembled laboratory scanner, as well as a synchrotron radiation based system, have been used. The experimental parameters, as well as the specific advantages of both systems, are presented.

Carcinogenic tissue of mice and rabbits enriched with magnetic nanoparticles has been measured by means of both tomographic setups. A direct comparison of the resulting datasets of the same sample underlines the advantages of synchrotron radiation based tomography in terms of spatial resolution, image quality and the possibility for resolving density differences. The evaluation of the datasets clearly shows a strong dependence of the distribution of particles within the tissue on the therapeutic approach. Furthermore, it is shown that quantitative information on the particle concentration can be determined by means of synchrotron radiation based tomography.

## 2. Biomedical applications of magnetic nanoparticles

### *2.1. Magnetic drug targeting (MDT)*

In cancer treatment, regular administration of chemotherapeutic agents is frequently associated with severe deleterious side-effects. Therefore, different approaches of regional drug delivery

systems have been developed to obtain a high concentration of the applied drugs in the respective carcinogenic region and to protect healthy tissue. In this context, MDT means the specific delivery of chemotherapeutic agents to their desired targets, e.g. tumours, by using magnetic nanoparticles (ferrofluids) bound to these agents and an external magnetic field which is focused on the tumour [4]. The magnetic particles, with their transported substances, will be travelling along the direction of the magnetic field gradient given by an external magnetic field. They will be held in position at the target region, thus preventing their flow with the blood stream. A prerequisite for the efficacy of this system is to reach the micro-circulation of the target-directed area and to release the active ingredient on a cellular or sub-cellular level [5].

We examined the possibilities for local cancer treatment by directing starch-coated magnetic nanoparticles labelled with the chemotherapeutic agent mitoxantrone to the target region using a constant magnetic field. The loaded magnetic nanoparticles were given intra-arterially into the tumour-supplying artery of tumour-bearing rabbits (VX2 squamous cell carcinoma) and focused in the tumour region by means of an electromagnet with a magnetic field strength of 1.7 T. With this delivery system, total tumour remissions without negative side-effects by the use of only 20% and 50% of the regular systemic chemotherapeutic dosage could be achieved [2]. $\gamma$-imaging with radioactive $^{59}$Fe-nanoparticles showed 114 times more activity in the tumour region after magnetic drug targeting compared to control without a magnetic field, as can be seen in [1]. Furthermore, it could be shown that, with this system, a high and specific enrichment of the bound chemotherapeutic agent in a desired body compartment (i.e. the tumour) is possible. High-performance liquid chromatography (HPLC) analysis of the chemotherapeutic agent after magnetic drug targeting revealed a 75 times higher concentration of the administered dose in the tumour region compared to the regular systemic administration [1].

### *2.2. Hyperthermia (HT)*

A second promising locoregional minimal-invasive approach for the treatment of tumours incorporating magnetic nanoparticles is tumour therapy by hyperthermia. The use of iron oxide nanoparticles for the local heating of tumours was proposed for the first time in the 1950s by Gilchrist *et al* [6]. The basic concept of hyperthermia is rather simple. In the first step, the magnetic material is applied by direct injection at the tumour site. Subsequently, the tissue is exposed to an AC magnetic field with frequencies on the order of the magnitude of 100 kHz. The magnetic moments of the nanoparticles now try to follow the direction of the alternating external field. Depending on the mean value of the particle size distribution, the specific magnetic loss power is dominated by Brownian or Neeliean relaxation of the magnetic moment of the particles. Thus, the alternating magnetic field can induce a rotational movement of the particles and the magnetic energy is converted into heat energy. Hence it is possible to elevate the temperatures of the tissue close to the injection site of the magnetic particles. The temperature that can be reached depends on the concentration and specific heating power of the magnetic material, as well as the parameters of the magnetic field. A number of studies show the principle possibility to reach a reduction of the respective tumour volume at treatment times of up to 12 min and temperatures of 43–55 °C [7, 8]. Considering the fact that, in this temperature regime, 50% of the tumours regressed only temporarily, Hilger *et al* incorporated a further increase in the temperatures at the target region. By means of this so-called 'magnetic thermo-ablation' approach, the target tissue is magnetically heated to values above 55 °C for several minutes in order to induce damage to the DNA which should lead to a complete destruction of the cellular structure.

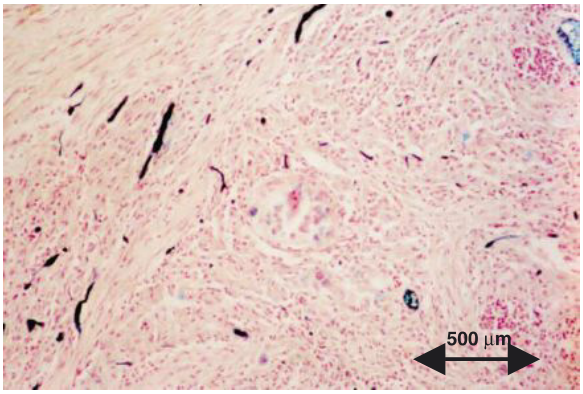


**Figure 1.** Cross section of a VX-2 carcinoma excised from a rabbit immediately after MDT. Magnetite particles have been stained by means of the Berlin blue reaction. Particles are mainly found in the tumour-supplying vessel system.

In order to demonstrate the feasibility of 'magnetic thermo-ablation', human breast carcinoma cells have been implanted into immunodeficient mice, as shown in [3]. After six weeks, magnetite-based ferrofluids with a mean particle diameter of 10 nm were injected intratumourally and the mice were exposed to an ac field with an amplitude of up to 6.5 kA $m^{-1}$ and a frequency of 400 kHz for up to four minutes. Using this procedure, intratumoural temperatures of up to 96 °C could be reached. A macroscopic shrinking of the tumours and the degeneration of their cellular structure after thermo-ablation could be shown by means of radioscopic imaging of the whole animal and microscopic examination of histological section of the tumour tissue, respectively.

## 3. Classical methods for determining magnetic particle distributions

### *3.1. Histological examinations*

The adsorption of magnetic material within the tumour region is commonly performed by means of microscopic examination of histological sections of the respective tissue. For the preparation of the histological section, the excised tissue is fixated in formaldehyde, dehydrated, and finally embedded in paraffin. Berlin blue staining of the histological section is used to achieve a labelling of the magnetite agglomerates within the tissue structure. Figure 1 shows an example of the histological cross section of a VX2-cell carcinoma excised from a rabbit immediately after MDT. The stained magnetite nanoparticles are located within the tumour-supplying vessels in the connective tissue.

Histological examinations offer the possibility of getting quantitative information about the particle concentration with a spatial resolution in the micrometre range. The resolution can be further extended to the nanometre range by using electron microscopy, as is shown, for example, in [9].

Classical histology is well established and a versatile method for the analysis of different kinds of tissue, but it is limited to two dimensions. It is nowadays possible to reconstruct 3D datasets using serial sectioning and image registration methods. However, the method is very time-consuming and tedious, and it is—due to its destructive nature—limited to *ex situ* examinations.

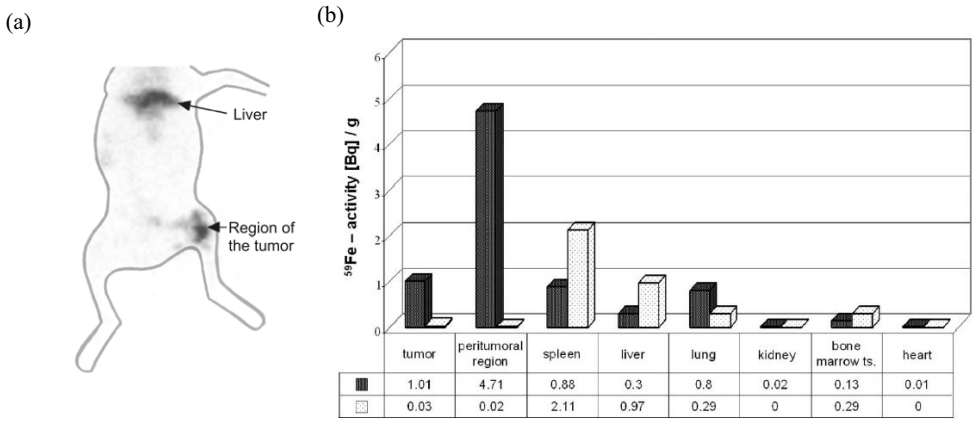


**Figure 2.** (a) The $\gamma$-image shows the distribution of magnetic nanoparticles within a tumour-bearing rabbit after mixing the carrier liquid of the particles with $^{123}$I. (b) Spatial distribution of radioactivity 60 min after inter-arterial application of $^{59}$Fe magnetic particles with (■) and without (□) the influence of an external magnetic field at the region of the tumour.

### *3.2. $\gamma$-ray radiography*

Imaging with $\gamma$-rays allows us to examine the distribution of magnetic material and its concentration *in vivo* during the application of the drug. Thus, it becomes possible to determine the time-dependent redistribution, and direct monitoring of the enrichment of the drug in different parts of the body becomes possible. Furthermore, a spatially resolved quantification of the particle concentration can be obtained.

The basic principle of $\gamma$-imaging is the detection of high-energy photons emitted from injected radionuclides inside the body using a gamma camera. It is therefore a prerequisite for this method to have radioactive labelling of the magnetic particles. For this purpose, the carrier liquid of the magnetic particles can be mixed with the radioactive gamma emitter, $^{123}$I. Another possibility is the use of the radioactive isotope $^{59}$Fe instead of natural $^{58}$Fe during the synthesis of the magnetic fluid. Figure 2 shows the distribution of magnetic material labelled with $^{123}$I within a tumour-bearing rabbit. The image was taken 40 min after application of the drug. Due to the external magnetic field localized at the tumour, an increased concentration of magnetic material at this region can be detected. By measuring the activity of Fe in different parts of the body, the significant influence of the magnetic field on the distribution within a test animal becomes obvious (figure 2(b)). The diagram shows that the external magnetic field gives rise to a very strong increase in the magnetic particle concentration at the tumour and the peritumoural region.

### *3.3. X-ray radiography*

X-ray absorption radiography can be used as a non-destructive tool to obtain qualitative and, if proper calibration is available, also quantitative information about the relative particle concentration. In contrast to $\gamma$-imaging, this technique requires no additional staining with radioactive material. The iron-based magnetic nanoparticles serve as a contrast agent, because they have much higher x-ray attenuation coefficients compared to biological tissue. Additionally, x-ray radioscopy generally provides much higher spatial resolution compared to $\gamma$-imaging.

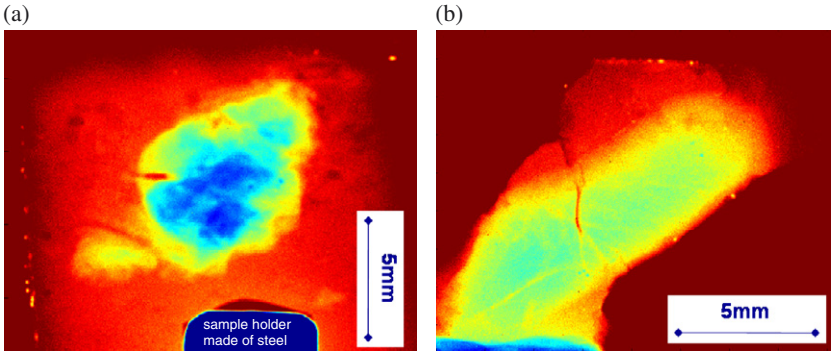


**Figure 3.** Radioscopic images of the tumour (a) and liver (b) of a mouse. The samples have been resected from the animal shortly (approximately 6 min) after an injection of magnetic nanoparticles into the tail vein of the animal. A high concentration of particles with an inhomogeneous distribution can be found in the necrotic centre of the tumour. The liver exhibits a much lower relative amount of particles with a more homogenous distribution.

*In vivo* as well as *in vitro* experiments are possible. In order to demonstrate the feasibility of this method, F9 cells (mouse teratocarcinoma) were implanted in immunodeficient mice. These cells develop rapidly growing and highly vascularized tumours. When the tumours reached a diameter of approximately 10 mm, a suspension of magnetic nanoparticles with a mean particle diameter of 10 nm was injected into the tail vein of the animal. Five to eight minutes later, the animals were sacrificed and the tumours, as well as the livers, were resected, fixated and subsequently embedded into paraffin. The radiographs in figure 3 show the typical x-ray absorption behaviour of the tumour and the liver of one of the test animals. The images were recorded by means of the laboratory x-ray setup presented in section 4.2 at a spatial resolution of 50 $\mu$m and a tube acceleration voltage of 20 kV. The radiograph of the tumour exhibits strong absorption of x-rays, which can be attributed to a high particle concentration. The highest concentration of magnetic material is located within the necrotic centre of the tumour. A qualitative comparison between the two radiographs (tumour and liver) indicates that the liver of the same animals contains a much lower concentration of magnetic material. Furthermore, the particles are distributed more homogenously.

## 4. Determination of magnetic particle distributions by means of x-ray tomography

X-ray tomography nowadays is a well-established standard tool for, for example, diagnostics in medical fields, non-destructive inspection and testing, or the three-dimensional analysis of the morphology of matter in various scientific fields such as geology, material science or biology [10, 11]. In the present work, x-ray tomography has been used for the three-dimensional imaging of different tumour models which have been enriched with magnetic nanoparticles.

The experiments were performed with two types of x-ray sources: a commercial tube on the one hand and a synchrotron on the other. In the following, the basic physical principles of the method, as well as the main features of the corresponding experimental setups, will be briefly outlined. Finally, the results of the examination of carcinogenic tissue enriched with magnetic nanoparticles are presented.

### *4.1. Physical background*

X-ray tomography allows the determination of the complete, i.e. also internal, three-dimensional morphology of an object without the need to perform a direct local measurement at each desired position. In order to carry out a tomographic scan, a set of radiograms—i.e. x-ray absorption images—of a sample at different projection angles $\Theta$ equally stepped between 0° and 360° are taken. A single projection is obtained by recording the primary intensity $I_0(x, z)$ and the attenuated intensity $I(x, z)$, where $x$ denotes the horizontal and $z$ the vertical dimensions. The attenuation projection at a specific angle, $P_\Theta(x, z)$, is given by the equation:

$$P_\Theta(x, z) = \int \mu(x, y, z)\, \mathrm{d}y = -\ln\left[\frac{I(x, z)}{I_0(x, z)}\right]. \tag{1}$$

The ensemble of all projections for all projection angles is referred to as the radon transformation of the object. The internal structure of the sample is implicitly contained in this transformation.

The tomographic reconstruction from the radiograms is achieved by inversing the radon transformation. In practice, this is commonly realised by calculating the backprojection of filtered projections by means of the BKFIL algorithm [12]. The resulting dataset, $\mu(x, y, z)$, represents the discrete function of the three-dimensional linear attenuation coefficient of the sample. Except for photon energy values close to absorption edges, this quantity is approximately described by:

$$\mu \propto \frac{Z^4}{E^3}\rho, \tag{2}$$

with $Z$ being the atomic number, $\rho$ the mass density and $E$ the photon energy. Thus, the reconstructed dataset is influenced by the composition of the examined object and the spectral properties of the probing radiation.

### *4.2. The laboratory x-ray scanner*

One part of the x-ray microtomography experiments has been carried out with a laboratory setup based on a commercial cone beam x-ray source (Apogee 5000) with 40 $\mu$m focus size and a maximal acceleration voltage of 50 kV. The x-ray beam passes the sample, which is mounted on a high-precision rotation stage and produces an absorption image of the sample on a phosphor screen (see figure 4(a)) with a sensitive area of $10 \times 10$ cm$^2$. By means of a macro-lens system, the images are transmitted to a low-noise $1024 \times 1024$ pixel (Marconi 47-10) CCD detector.

X-ray tubes generally have a divergent cone-shaped emission characteristic. It is therefore possible to realize different magnifications of the object by a variation of its relative position between sample and detector. The magnification $m$ is given by $m = D/R$, with $R$ being the distance between source and sample and $D$ between source and detector. The cone-beam geometry has to be taken into account for the reconstruction of the dataset by, for example, using the adapted version of the BKFIL algorithm developed by Feldkamp *et al* [13].

Due to the much lower photon flux provided by x-ray tubes (compared to a synchrotron radiation source), the tomographic datasets from the laboratory system generally feature a higher noise level. Additionally, the polychromatic nature of the emission spectrum gives rise to so-called beam-hardening artefacts, which are a severe problem for a quantitative density determination. With a polychromatic source, the energy dependence of the linear attenuation coefficient $\mu$ has to be taken into account. Hence, the attenuated intensity $I(x, z)$ is a function

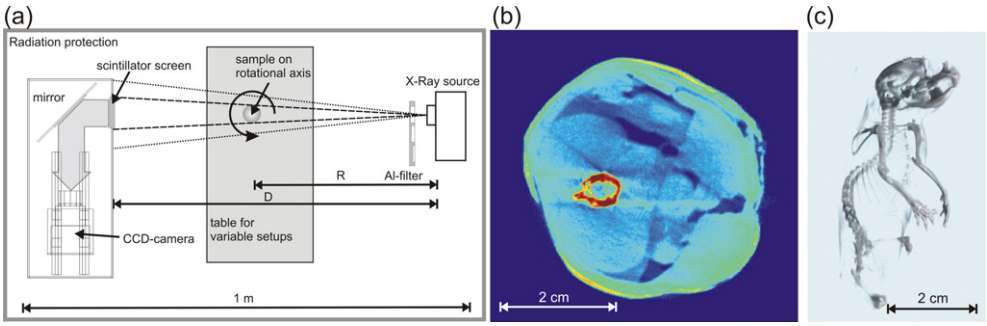


**Figure 4.** The drawing (a) shows the schematic setup of the laboratory x-ray scanner. The size of the phosphor screen ($10 \times 10$ cm$^2$) and the divergent beam allows for the scanning of larger objects in comparison to the system based on synchrotron radiation shown in figure 5. As an example, the axial slice of the tomographic dataset of a mouse is shown in (b). The radial density gradient is caused by beam hardening of the polychromatic spectrum of the x-ray tube. Thus, only the segmentation of matter having a large density difference (bones and soft tissue) can be performed. The rendered image (c) shows the skeleton of a mouse after segmentation of the dataset.

of the photon energy $E$ of the x-ray source:

$$I(x, z) = \int I(E) \exp\left[\int \mu(y, E)\, \mathrm{d}y\right] \mathrm{d}E. \tag{3}$$

The effect of the energy dependence of $\mu$ on the tomographic reconstruction is shown in figure 4(b). The example shows an axial slice of the tomogram of a mouse, which has been obtained by means of the tube-based laboratory system. When the incoming polychromatic beam hits the sample, its spectral distribution is modified. As described by equation (2), the lower energetic part of the spectrum experiences higher absorption. Inner parts of the samples are therefore penetrated by radiation whose spectrum has been altered in a way that the mean energy of the incident spectrum is lower than that of the exit spectrum. However, the reconstruction algorithm which calculates $\mu(x, y, z)$ from the projection images assumes that the attenuation coefficient does not depend on the x-ray energy. Therefore, the tomograms of datasets that have been reconstructed from absorption images obtained with a polychromatic source feature a radial density gradient. The modification of the energy spectrum gives rise to the apparently higher density of the parts close to the sample surface facing the source, as can be seen clearly in figure 4(b). In conclusion, it is only possible to perform a segmentation of materials with a high density difference, such as bones and soft tissue, as is shown in figure 4(c). It is principally possible to reduce beam-hardening artefacts, e.g. by incorporating filters which accomplish a pre-hardening of the x-ray spectrum or by taking into account the energy dependence of the x-ray attenuation [12]. Nonetheless, a quantitative evaluation of the density distribution from tomographic datasets measured by means of a polychromatic source is limited to rather simple two-phase systems such as solid foams. In the case of multiphase and complex structures such as biological specimens, it is hence favourable to incorporate an x-ray source which offers the possibility of performing measurements with monochromatic radiation.

### *4.3. Synchrotron radiation based micro-computed tomography (SR$\mu$CT)*

The extremely high intensity of monochromatic synchrotron radiation gives the opportunity to get almost noise-free tomography datasets with a very high spatial resolution, which nowadays

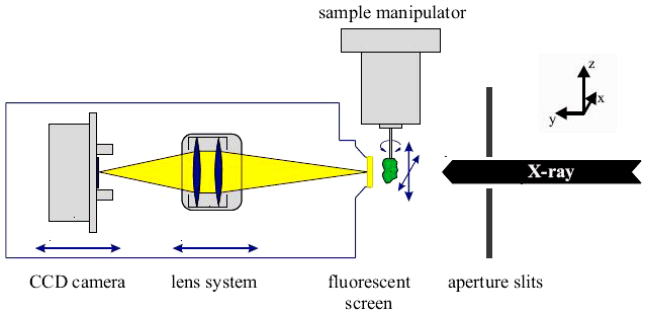


**Figure 5.** Schematic drawing of the apparatus for the synchrotron radiation based tomography measurements [18].

reaches values of typically down to 1 $\mu$m in combination with absorption contrast sensitivity. As can be seen from equation (2), for the case of monochromatic radiation the attenuation coefficient $\mu$ only depends on the atomic composition and the density of the sample. Thus, a quantitative determination of the spatial density distribution becomes possible. Due to these advantages, SR$\mu$CT has become a versatile tool for quantitative 3D imaging, which has been used in a variety of biomedical studies [10]. Examples of the successful application in this context are the analysis of the bio-compatibility of implants, the visualization of the capillary system of the myocardium, or the observation of the failure behaviour of bones [14–16].

The SR$\mu$CT measurements for the present work were performed at the HASYLAB beamline BW2 at the storage ring DORIS III of DESY in Hamburg. At this wiggler beamline, a double-crystal monochromator (Si(111)-crystals) provides photon energies in the range of about 8–24 keV, which is suitable for the investigation of low-absorbing materials such as biological tissue or polymers.

The setup used for absorption-contrast microtomography is presented schematically in figure 5. It consists of a two-dimensional x-ray detector and a sample manipulator stage. The sample manipulator provides both rotation as well as lateral positioning of the specimen.

The cross-sectional area of the beam provides a maximum field of view of about 3.5 $\times$ 10 mm$^2$. The vertical and horizontal position of the sample can be changed with respect to the beam in order to examine specimens which are larger than the maximum area of the projected beam.

For measurement of the absorption images of the specimen, the incident x-ray beam is converted into visible light using a $CdWO_4$ single-crystal scintillator which is projected onto a CCD camera (Apogee KX2 with 1536 $\times$ 1024 pixels; pixel width, 9 $\mu$m) by means of an optical lens system with a focal length of 50 mm. As the emission characteristics of synchrotron radiation is almost parallel, the absorption images on the scintillator screen have to be magnified by the lens in order to overcome the limit of 9 $\mu$m given by the pixel size of the CCD. The lens system provides a magnification range between 0.7 and 6. Thus the effective pixel size of the visible absorption images on the scintillator screen can be adjusted between 13 and 1.5 $\mu$m. The spatial resolution of the detectors system is defined by the so-called modulation transfer function (MTF) [17], which can be described pictorially as the detectable number of line-pairs per millimetre. The maximum spatial resolution, which can be reached by means of the system shown in figure 5, is approximately 2 $\mu$m. Depending on the desired spatial resolution, the step size for the projection angle is chosen to be between 0.5° and 0.25°. Due to the parallel beam geometry, it is only necessary to measure projections from the angular interval between 0° and 180°, i.e. up to 720 absorption images are recorded for one tomographic scan.

More details about the properties of the tomography system at HASYLAB can be found in [18].

## 5. Results

Two different kinds of tumour samples have been prepared for the experiments in order to demonstrate how the location of the application of the drug affects the distribution of the particles within the tissue:

(1) Sample tissue with intratumoural particle injection for hyperthermia (HT) resected from tumour-bearing mice.
(2) Sample tissue with intravascular particle injection for magnetic drug targeting (MDT) resected from tumour-bearing rabbits.

In both cases, the tumours were resected from the animals after the respective therapy was finished. The tissue samples were fixated in formalin and subsequently embedded into paraffin.

Figure 6 shows an axial slice as well as a rendered 3D representation of the dataset of a tumour after intratumoural particle injection (HT sample). At the centre of the sample, the channel of the injection needle can be identified.

For the SR$\mu$CT tomograms, $\mu$ is represented by 8-bit unsigned integer values, i.e. the maximum absorption value of a dataset equals 255. The size of the overall cylindrically shaped sample (tumour tissue and paraffin bed) was about 5 mm in diameter and 4 mm in height. The SR$\mu$CT scan was performed at a photon energy of 24 kV with an optical magnification of 2.4. With these settings, a voxel size of 3.5 $\mu$m and a spatial resolution of approximately 5 $\mu$m were obtained. As mentioned above, the numerical inversion of the radon transformation of the object (i.e. the ensemble of x-ray absorption images from different viewing angles) reconstructs the corresponding three-dimensional distribution of the linear attenuation coefficient, $\mu(x, y, z)$, in terms of voxels on a Cartesian grid. The grey-value distribution of the attenuation coefficient is plotted as a histogram in figure 6(c). As is indicated in the plot, it can be divided into three main parts. The structures of the tomogram which belong to each of these sections are shown in the three rendered images located above the diagram. The first very sharp peak (I) represents the weak x-ray absorption of the air surrounding the paraffin block and the sample during the measurement. The second peak (II) corresponds to the attenuation behaviour of the paraffin and the biological tissue with a vanishing or very low concentration of magnetic material. Due to the fact that the attenuation coefficient of these components is rather similar, it is not possible to perform a complete quantitative segmentation.

It is, however, straightforward to separate the third peak (III) from the rest of the dataset. As is shown in figure 6(c), the minimum value between the second and third peaks has been chosen as the threshold value for the segmentation procedure. The remaining voxels in the dataset belong to the area of the tumour tissue close to the injection site of the nanoparticles. Within a radius of about 1 mm of this position, the highest x-ray attenuation values of the dataset can be found. It is obvious that the absorption within this area can mainly be traced back to a high relative concentration of magnetic particles. It reaches maximum values at a distance of about 200–300 $\mu$m. With increasing distance, the concentration becomes lower and drops sharply at the border of the necrotic centre of the tumour. No staining of the vessel's systems within the outer region of the tumour can be observed. Thus it can be concluded that the particles predominantly remain close to the injection site and do not diffuse into the peritumoural area or beyond. Regarding the influence of the particle distribution on the success of the hyperthermia therapy, this is a promising result, as the efficacy of the heat generation

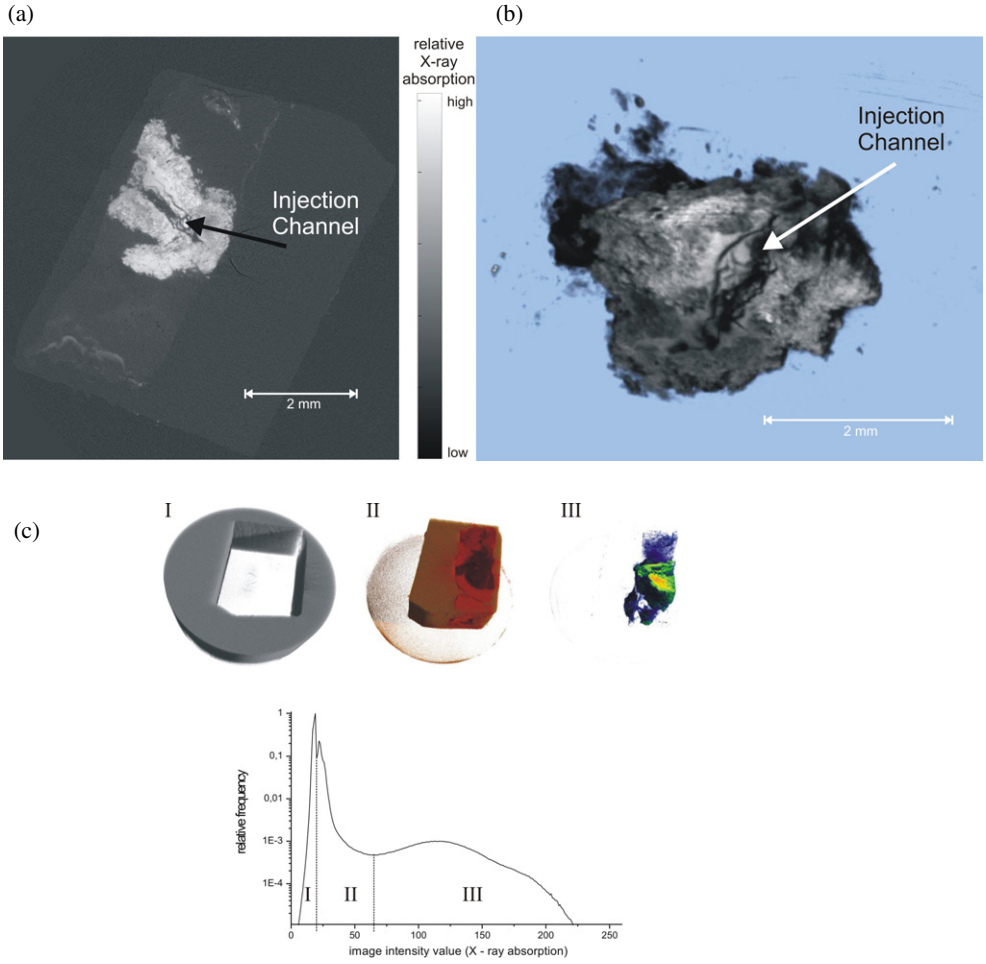


**Figure 6.** ((a), (b)) SR$\mu$CT dataset of a tumour extracted from a mouse enriched with magnetic nanoparticles applied by means of intratumoural injection (HT sample). (c) The histogram of the x-ray absorption coefficient has been divided into three parts. The insets above the plot show the volume of the datasets which correspond to each of these parts. The magnetic material causes much higher x-ray absorption than the rest of the sample (section III of the histogram). It is localized in a confined area close to the injection site.

of this method is strongly influenced by the concentration of magnetic material within the tissue.

The images in figure 7 show the tomogram of the section of a tumour excised from a rabbit after MDT which originally had a volume of approximately $20\times20\times40\,\mathrm{mm}^3$. As the maximum width of the synchrotron beam was about 15 mm, a piece with a size of $10 \times 10 \times 15\,\mathrm{mm}^3$ was cut from the centre of the sample. The measurement was performed at a photon energy of 18 keV with an optical magnification of 1.36. With these parameters, a spatial resolution of about 10 $\mu$m could be obtained.

Already, at a first glance, the dataset reveals the completely different character of the particle distribution within the tissue compared to that observed after the intratumoural injection. As can be seen from the axial section (a), the vessel system of the sample can clearly

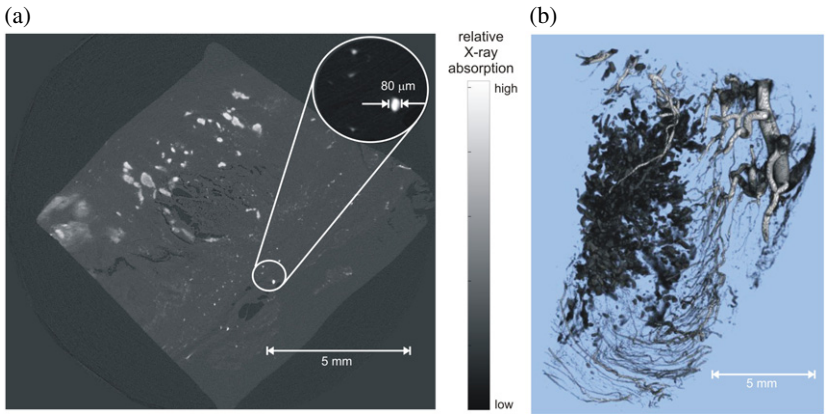


**Figure 7.** Representations of SR$\mu$CT datasets of carcinogenic tissue extracted from a rabbit after MDT. The nanoparticles have been applied by means of intravascular injection close to the tumour. The highest concentration of magnetic material can be found within the vessel system.

be differentiated from the surrounding tissue, as it shows significantly higher x-ray attenuation compared to the surrounding tissue or the paraffin bed. The rendered 3D representation in (b) shows the remaining structure of the sample after a segmentation of the dataset. Only the voxels having an attenuation value above a certain threshold (given by the minima between the two major peaks of the histogram of the attenuation coefficient) remain visible. It becomes obvious that the magnetic material is mainly confined to the capillaries, i.e. the blood supply system of the tumour. The finest capillaries, which can be identified from the tomogram, have a diameter of about 20 $\mu$m. A second prominent feature of the dataset is the irregularly shaped cloud-like structure, which dominates the left section of the dataset (cf figure 7(b)). The attenuation coefficient of this structure is significantly lower than the average value of the vessel system. Furthermore, it shows stronger x-ray absorption than unstained tissue or paraffin. Additional information is required to identify the origin for the cloud-like structure. Thus a microscopic analysis of histological cuts of the respective region is planned in the near future.

The two different tumour samples (HT and MDT) have also been scanned by means of the conventional laboratory setup to underline the advantages of SR$\mu$CT in terms of spatial resolution, image quality and the possibility of resolving density differences. For the conventional CT measurements, the setup described in section 4.2 was employed. Both samples were scanned at a magnification factor of $m = 3$ with a tube acceleration voltage of 30 kV. The resulting effective voxel size of the tomographic dataset is about 50 $\mu$m.

Axial slices from the datasets of both samples obtained with the two different tomography setups are displayed in figure 8. As indicated in the images, the conventional data has been scaled by the factor which corresponds to the ratio of the effective pixel size from the SR$\mu$CT and the conventional CT measurements. Two conclusions can be drawn from the qualitative comparison of the datasets: firstly, SR$\mu$CT offers higher spatial resolution, i.e. more detail about the geometric structure of the samples can be obtained. Due to these artefacts, secondly, the spatial distribution of the attenuation coefficient deviates from the data obtained by means of the monochromatic synchrotron source. This effect can be attributed to the hardening of the spectrum of the polychromatic source of the conventional system (cf section 4.2). Accordingly, for quantitative determination of the density distribution, it is preferable to incorporate SR$\mu$CT measurements.

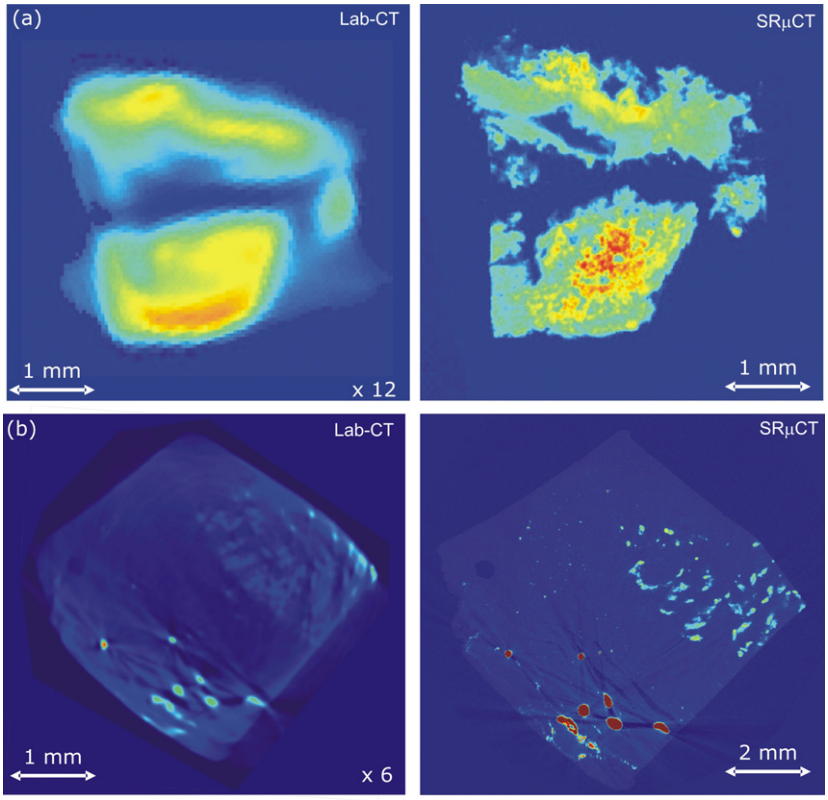


**Figure 8.** The axial slices of HT (a) as well as MDT tumour samples indicate the advantages of SR$\mu$CT in comparison with conventional CT examination by means of the laboratory setup (cf section 4.2).

## 6. Outlook

### *6.1. Quantitative determination of the particle concentration*

As described in section 4.3, the linear x-ray attenuation coefficient for monochromatic sources only depends on the composition and the density of the examined sample. Therefore, it is principally possible to derive a quantitative three-dimensional density map from SR$\mu$CT datasets.

Of major relevance for a further improvement of MDT as well as hyperthermia is knowledge of the absolute concentration of magnetic material within a specific tissue area. One possible approach for the determination of the Fe concentration from SR$\mu$CT measurements is demonstrated in figure 9. The goal of this simple experiment was to obtain a calibration curve which relates the attenuation coefficient to the iron concentration within a sample. For this purpose, six suspensions of iron-based particles with an Fe concentration in the range between 11.25 and 360 $\mu$g ml$^{-1}$ have been prepared. For the tomography measurements, the suspensions have been filled into plastic canulas with an inner diameter of 2.5 mm. Figure 9(a) shows the histogram of the attenuation coefficient as well as an axial slice of the corresponding dataset obtained from the tomogram of the sample with the highest iron concentration. The distribution features three narrow Gaussian peaks which can be attributed

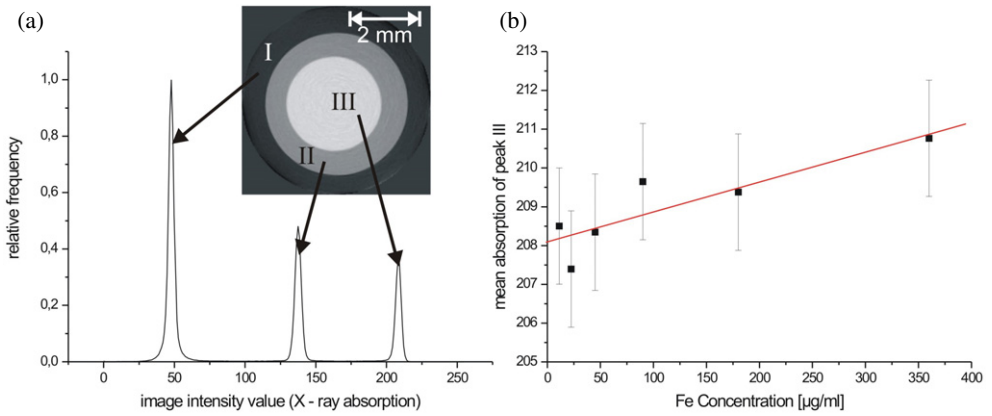


**Figure 9.** Histogram of the x-ray attenuation behaviour of a suspension of iron-based nanoparticles contained in a plastic canula (a). The mean attenuation value has been determined for six suspensions with different iron particle concentrations (b).

to the air (I) surrounding the sample container during the measurement, the polymer (II) of the sample container, as well as the suspension of nanoparticles (III). The mean attenuation value of the suspension (peak III) has been calculated and plotted against the respective Fe concentrations, as shown in figure 9(b). The error bars represent the corresponding standard deviation. A linear regression was used to gain the first approximation for the calibration function, which describes the relation between the x-ray attenuation behaviour and the iron content of the suspension samples. The plot clearly shows an increase in the attenuation coefficient of the suspension with growing Fe concentration.

In the future it is planned to apply this calibration method for the determination of a three-dimensional map of the particle concentration within tumour samples.

### *6.2. The new tomography system at HASYLAB*

A multipurpose, ultra-fast and high-resolution micro tomography system, which will be an important part of the new GKSS material science beamline HARWI 2, is currently under construction. The wide energy range (20–250 keV), large beam geometry ($10 \times 70$ mm$^2$) and spacious and heavy load sample environment will allow a unique variety of experiments, from material science to biomedical observations. The new tomography system consists of two main components, the detector and the sample positioning system, which additionally can be combined with a detector unit for x-ray diffraction. Both methods (tomography and diffraction) can be used simultaneously.

The tomography detector is designed to allow a high resolution of $\approx 2$ $\mu$m and below, as well as ultra-fast tomography with a scanning time of below 10 s, for a whole tomogram at a spatial resolution of below 40 $\mu$m. The optical lens system covers a reproduction scale between $0.5\times$ to $6\times$. Thus, using the lowest magnification the whole beam size can be observed, whereas at the highest magnification the maximum resolution can be reached.

In order to provide high flexibility for the experiments, the sample positioning system consists of two stages. The lower part contains a coarse lifting table, and two high-precision and heavy-load Huber manipulators. The linear stage features a $y$-travel range of 400 mm and the lifting table a $z$-range of 90 mm, respectively. Moreover, this system can carry a load of up to 150 kg and thus allows the installation of heavy and spacious experimental environments up

to a size of about $400 \times 400 \times 400\,\mathrm{mm}^3$. For tomographic examinations that require no special sample treatment, a rotary table and an $xy$-table are mounted on top of the system.

Due to the unique combination of properties of the HARWI-2 beam and the new tomography system, a large number of experiments become possible. The wide energy range allows the analysis of high absorbing materials (for example, steel samples) just as well as large biomedical soft-tissue samples. Various experiments from very different research areas which use the capabilities of the new system are already planned.

The next steps that are related to the project of the present work will be the examination of larger samples such as complete rabbit tumours and whole animals. The latter will provide three-dimensional and quantitative information about the distribution of the particles within different parts of the body. Furthermore, it is planned to perform *in vivo* studies in order to examine the time-dependent behaviour of particle propagation after the application of the nano-particles for MDT or hyperthermia.

## Acknowledgment

This project is funded by DFG SPP1104.

## References

[1] Alexiou C *et al* 2003 Magnetic drug targeting—biodistribution of the magnetic carrier and the chemotherapeutic agent mitoxantrone after locoregional cancer treatment *J. Drug Targeting* **11** 139–49
[2] Alexiou C *et al* 2000 Locoregional cancer treatment with magnetic drug targeting *Cancer Res.* **60** 6641–8
[3] Hilger I *et al* 2001 Electromagnetic heating of breast tumors in interventional radiology: *in vitro* and *in vivo* studies in human cadavers and mice *Radiology* **218** 570–5
[4] Gupta P K and Hung C T 1994 Magnetically controlled targeted chemotherapy *Microspheres and Regional Cancer Therapy* ed N Willmott and J Daly (Boca Raton, FL: CRC Press) pp 71–116
[5] Widder K J, Senyei A E and Ranney D F 1979 Magnetically responsive microspheres and other carriers for the biophysical targeting of antitumor agents *Advances in Pharmacology and Chemotherapy* ed S Gavattini *et al* (New York: Academic) pp 213–39
[6] Gilchrist R K *et al* 1957 Selective inductive heating of lymph nodes *Ann. Surg.* **146** 596–606
[7] Murray T G, Steeves R A and G L 1997 Ferromagnetic hyperthermia: functional and histopathologic effects on normal rabbit ocular tissue *Int J. Hyperthermia* **13** 423–36
[8] Chan D C F, Kirpotin D B and Bunn P A 1993 Synthesis and evaluation of colloidal magnetic iron oxides for the site-specific radiofrequency-induced hyperthermia of cancer *J. Magn. Magn. Mater.* **122** 374–8
[9] Alexiou C *et al* 2006 Targeting cancer cells: magnetic nanoparticels as drug carriers *Eur. Biophys. J.* doi:10.1007/s00249-006-0042-1
[10] Bonse U 2004 *SPIE: Developments in X-Ray Tomography IV (Denver)*
[11] Baruchel J, Buffiere J-Y, Maire E, Merle P and Gilles P 2000 *X-Ray Tomography in Material Science* (Paris: Hermes Science Publications)
[12] Kak A C and Slaney M 1999 *Principles of Computerized Tomographic Imaging* (New York: IEEE)
[13] Feldkamp L A, David L and Kress J 1984 Practical cone beam algorithm *J. Opt. Soc. Am.* **1** 612–9
[14] Müller B, Fischer J, Dietz U, Thurner P and Beckmann F 2006 Blood vessel staining in the myocardium for 3d visualization down to the smallest capillaries *Nucl. Instrum. Methods Phys. Res.* B **246** 254–61
[15] Müller R and Nazarian A 2004 Time-lapsed microstructural imaging of bone failure behavior *J. Biomech.* **37** 55–65
[16] Thurner P, Müller B, Sennhauser, Hubbell J and Müller R 2004 Tomography studies of biological cells on polymer scaffolds *J. Phys.: Condens. Matter* **16** S3499–510
[17] Schneiders N J and Bushong S C 1978 Single-step calculation of the MTF from the ERF *Med. Phys.* **5** 31–3
[18] Donath T, Beckmann F, Heijkants R G J C, Brunke O and Schreyer A 2004 Characterization of polyurethane scaffolds using synchrotron radiation based computed tomography *SPIE: Developments in X-Ray Tomography IV (Denver)*